SPHERICAL HARMONIC ANALYSIS OF STEADY PHOTOSPHERIC FLOWS

DAVID H. HATHAWAY

Space Science Laboratory, NASA Marshall Space Flight Center, Huntsville, AL 35812, U.S.A.

Abstract. Steady photospheric flows can be represented by a spectrum of spherical harmonic modes. A technique is described in which full disc doppler velocity measurements are analysed using the spherical harmonic functions to determine the characteristics of this spectrum and the nature of these flows. Synthetic data is constructed for testing this technique. This data contains limb shift, rotation, differential rotation, meridional circulation, supergranules, giant cells and various levels of noise.

The data is analysed in several steps. First, the limb shift is calculated by finding the average velocity in concentric rings about disc center. A polynomial representation of the limb shift is then removed from the data. Secondly, the rotation profile is calculated by finding an average slope in the velocity across the disc at each latitude position. This rotation profile is fit with Legendre polynomials and removed from the data. The third step is to find the meridional circulation by calculating the spherical harmonic transform for the axisymmetric poloidal modes and correcting for the effects of the limb shift analysis. The final step is to calculate the full spectrum of spherical harmonic components for the convective flows. Supergranules are separated from giant cells by spectral filtering for high ($l > 32$) and low ($l < 32$) wavenumbers, respectively.

Some information about the spectrum is lost because only one hemisphere is seen, only the line-of-sight velocity is measured and the measurements contain noise. The lack of information about the motions on the backside of the Sun produces a broad smearing of the spectrum into nearby modes. The lack of information about the transverse velocity component produces a mixing between modes whose longitudinal wavenumbers differ by two and between the poloidal and toroidal components with the same wavenumber. In spite of this mode mixing much can be learned from this analysis. Solar rotation and differential rotation can be accurately measured and monitored for secular changes. Meridional circulations with small amplitudes can be measured and monitored and giant cells can be separated from supergranules.

1. Introduction

Much excitement has been generated recently by the use of the acoustic oscillation modes of the Sun for probing the structure and dynamics of the solar interior. Yet, much still remains to be learned about the 'steady' motions in the photosphere itself. While these surface flows are not easily measured using the acoustic modes, the Doppler measurements required for the oscillation studies yield explicit information on these flows when averages are taken over several oscillation periods. Measurements and monitoring of steady photospheric flows can be carried out in conjunction with the *p*-mode observations and can complement measurements of the solar internal structure and dynamics with data points at the photosphere itself.

The discovery of torsional oscillations of the Sun by Howard and LaBonte (1980) indicates that exciting discoveries may yet be uncovered in the steady flows of the solar photosphere. Giant cells, convective elements that span the convection zone, were proposed years ago by Bumba and Howard (1965) and Simon and Weiss (1968) and yet their existence is still in question. Although there is strong theoretical support for

the existence of giant cells, the observational support is weak. There are also gaps in our knowledge about supergranules. Hathaway (1982) has shown that the solar rotation may produce cyclonic motions in the downdrafts around the borders of the super-granules and produce latitudinal variation in supergranule flows, but observational evidence for these effects is still lacking. The nature of the Sun's meridional circulation also remains uncertain. Answers to these questions might be forthcoming if the different components of the steady photospheric flows could be measured on an hourly or even a day to day basis.

During the years of searching for giant cells a variety of techniques have been used. In general these techniques fall into one of two categories – temporal averaging or spatial averaging. These techniques are required to remove the 'noise' due to the strong signal from the supergranules. In the temporal averaging method a point on the Sun can be observed for about two weeks during its passage across the disc. However, averaging these observations together does not effectively remove the supergranules. Since supergranules have lifetimes of 1 or 2 days, Worden and Simon (1976), something less than about ten supergranules will have evolved at any point over that period of time. This would give an reduction of the supergranule signal by only about a factor of three. In the spatial averaging method a running mean is taken over the observed velocity field with apertures of various shapes and sizes. This method is also ineffective in removing the supergranules. If the aperture has a diameter of 100 000 km it covers only about ten supergranules – again giving a reduction of only about a factor of three. Larger apertures would begin to average over the giant cells themselves. These deficiencies suggest that some other analysis technique is required.

Here a new approach is described in which the supergranules are fully resolved and are separated from giant cells by their spatial characteristics. The spherical harmonics are used to provide a representation of all of the steady flows. Rotation, differential rotation and meridional circulation are represented by the axisymmetric or zonal harmonics. Supergranules and giant cells are represented by a spectrum of non-axisymmetric components. Snodgrass (1984) has made an important contribution in this direction by proposing the use of orthogonal functions for separating the different flow components. However, his analysis includes only the limb shift and the axi-symmetric modes and is not carried out for the supergranules and giant cells. He also used different functions for the rotation and for the meridional circulation when both can be represented by the spherical harmonics.

Here the spherical harmonics are used as the natural representation of flows in the photosphere. Although the loss of information about flows on the backside of the Sun and about the components of the flow transverse to the line-of-sight does compromise the orthogonality of these functions, they can be used to successfully separate the different flow components and provide information about the details of the flows on the surface. Solar rotation, differential rotation, and meridional circulations are uniquely represented by the spherical harmonics. Supergranules and giant cells can be separated by examining the high-wavenumber and low-wavenumber regions of the spherical harmonic spectrum without resorting to spatial or temporal averaging.

In the following section the nature of the data to be used in this analysis is described and the data requirements are discussed. Synthetic data is constructed for testing the analysis technique. The synthetic data construction is described in Section 3 and the analysis technique is presented in Section 4.

2. Data Requirements

Several requirements and constraints need to be made on the type of data that will be analysed with this technique. The basic requirement is for spatially resolved full disc observations for the line-of-sight component of the steady flows in the solar photophere. The lack of information about flows on the backside of the Sun introduces a mixing between different components of the flow such that the measured amplitudes are changed. The magnitude and nature of this mixing will be examined in Section 4. If the observations cover less than the full disc this mixing between different modes will be more severe. If intensities or magnetic fields are the measured quantities the method would need to be altered, e.g., Stenflo and Vogel (1986).

The spatial resolution requirement cannot be determined *a priori*. One would expect that the supergranules should be well resolved in order to accurately determine their spectrum. This would require a resolution of a few arc sec or less. Experiments can be undertaken to determine the effects of different spatial resolution on the analysis technique. Such experiments will be described in a later paper.

The temporal resolution is more easily fixed by the presence of the 5 min oscillations. Observations must be taken about once a minute to resolve these motions and then averaged over several cycles to remove this oscillatory signal from the steady flows. Hill (1986) has investigated this problem by taking successively longer averages of a series of velocity observations taken at 63 s intervals. He finds that after about 1 h the differences between the averages is reduced to a level of about 5 m s^{-1} at each $1'' \times 1''$ pixel. Careful attention must be taken in making these averages with high spatial resolution data since the Sun's rotation translates the flows across the disc. In addition to the 5 min oscillations there may be other intrisically solar noise at longer periods, e.g., g-modes and mesogranulation. This 'noise' would then be included as signal for the analysis presented here depending upon the spatial resolution and the length of the temporal averaging.

Another useful requirement for the data is to have the solar rotation axis aligned with one dimension of the data array. Although the data array can be rotated in software to fulfill this requirement, the process introduces noise which could be avoided if the alignment is made at the time of data acquisition. The analysis proceeds by also assuming that the solar rotation axis is in plane of the sky and then transforming the spectrum afterward to account for the tilt of the axis toward or away from the observer.

3. Synthetic Data Construction

In order to test the analysis technique synthetic data is constructed to represent the actual observations. Here it is assumed that the solar rotation axis is in the plane of the

sky. A spherical polar coordinate system is used with the polar angle, θ, measured from the north pole and the azimuthal angle, ϕ, measured from the east limb toward the west. The line-of-sight velocity component, V, is calculate at each pixel position. This synthetic data includes the convective limb shift, solar rotation and differential rotation, a meridional circulation, supergranules, giant cells, and a component of random noise, In order to resolve the supergranules a 256 by 256 array is used to construct the image.

The convective limb shift component is assumed to be independent of latitude and depends only on the radical distance, r, from disc center (where $r = 1$ at the limb). A simple parabolic profile is used with

$$V(r) = 300-400r^2 \text{ m s}^{-1}.$$

(3.1)

The other velocity components can be calculated from a spherical harmonic representation of velocity fields on the surface of a sphere (e.g., Chandrasekhar, 1961, p. 225). These flows are assumed to be in the horizontal with no radial component. Such flows are characterized as poloidal if the curl of the flow component vanishes and as toroidal if the divergence vanishes. The horizontal velocity components are given by

$$U_\theta(\theta, \phi) = \sum_{l, m} \left[S_l^m \frac{\partial Y_l^m}{\partial \theta} + T_l^m \frac{1}{\sin \theta} \frac{\partial Y_l^m}{\partial \phi} \right],$$

(3.2)

$$U_\phi(\theta, \phi) = \sum_{l, m} \left[S_l^m \frac{1}{\sin \theta} \frac{\partial Y_l^m}{\partial \phi} - T_l^m \frac{\partial Y_l^m}{\partial \theta} \right],$$

(3.3)

where the $Y_l^m(\theta, \phi)$ are the sperical harmonics with

$$Y_l^m(\theta, \phi) = \overline{P}_l^m(x)e^{im\phi}$$

(3.4)

and the $\overline{P}_l^m(x)$, where $x = \cos \theta$, are the normalized associated Legendre polynomials of degree l and order m (e.g., Abramowitz and Stegun, 1964). These polynomials can be generated recursively using

$$\overline{P}_l^m(x) = \left[\frac{(2l + 1)(2l - 1)}{(l + m)(l - m)} \right]^{1/2} x \, \overline{P}_{l-1}^m(x) -$$

$$- \left[\frac{(2l + 1)(l + m - 1)(l - m - 1)}{(2l - 3)(l + m)(l - m)} \right]^{1/2} \overline{P}_{l-2}^m(x)$$

(3.5)

with

$$\overline{P}_{m-1}^m(x) = 0 \quad \text{and} \quad \overline{P}_m^m(x) = \left[\frac{1}{2} \frac{3 \times 5 \cdots (2m + 1)}{2 \times 4 \cdots (2m)} \right]^{1/2} (1 - x^2)^{m/2}$$

(3.6)

as starting values. This recursion relation is stable and efficient in that no intermediate results are calculated when producing polynomials of the same order m but different

degrees for the Legendre transforms. The spectral coefficients for the poloidal modes are given by the S_l^m while the coefficients for the toroidal modes are given by the T_l^m. Since the velocity calculations involve derivatives of the spherical harmonics it is useful to know that

$$\frac{\partial Y_l^m}{\partial \theta} = -\sin\theta \frac{\mathrm{d}\bar{P}_l^m}{\mathrm{d}x} e^{im\phi} \tag{3.7}$$

with

$$\frac{\mathrm{d}\bar{P}_l^m}{\mathrm{d}x} = \frac{mx}{(1-x^2)^{1/2}} \bar{P}_l^m(x) - [(l+m+1)(l-m)]^{1/2} \bar{P}_l^{m+1}(x). \tag{3.8}$$

Solar rotation is represented by the toroidal axisymmetric ($m = 0$) modes with

$$U_\theta(x) = 0 \quad \text{and} \quad U_\phi(x) = \sum_l T_l^0 [l(l+1)]^{1/2} \bar{P}_l^1(x). \tag{3.9}$$

Using a rotation profile like that found by Howard and Harvey (1970) with

$$U_\phi(x) = 2000(1 - 0.126x^2 - 0.159x^4)(1 - x^2)^{1/2} \, \mathrm{m \ s}^{-1} \tag{3.10}$$

gives

$$T_1^0 = 1569.585, \qquad T_3^0 = -33.070, \qquad T_5^0 = -3.444, \tag{3.11}$$

with all the other components vanishing.

The meridional circulation is represented by the poloidal axisymmetric modes with

$$U_\theta(x) = -\sum_l S_l^0 [l(l+1)]^{1/2} \bar{P}_l^1(x) \quad \text{and} \quad U_\phi(x) = 0. \tag{3.12}$$

Using a simple meridional circulation directed towards the poles from the equator with

$$U_\theta(\theta) = -40 \sin\theta \cos\theta \, \mathrm{m \ s}^{-1} \tag{3.13}$$

gives

$$S_2^0 = 8.433, \tag{3.14}$$

with all the other components vanishing.

The convective flows, supergranules and giant cells, will in general contain both poloidal and toroidal components. The poloidal components represent the overturning motions which manifest themselves at the surface as horizontal flows from updraft regions to downdrafts. The toroidal components represent cyclonic and anticyclonic swirling motions.

The supergranules are represented in the synthetic data by a spectrum of modes all with degree $l = 100$ but with order $m = 10, 20, 30, \ldots, 100$. For $m = 10$ to 90 the poloidal and toroidal amplitudes are:

$$S_{100}^m = 1.0, \qquad T_{100}^m = 0.1, \tag{3.15}$$

for $m = 100$

$$S_{100}^{100} = 0.7, \qquad T_{100}^{100} = 0.07. \tag{3.16}$$

This spectrum gives a cellular pattern of about the right size for supergranules with maximum flow velocities of about $500\ \mathrm{m\ s^{-1}}$. Figure 1 shows the line-of-sight component of this combination of modes. Note that for the poloidal component the lines through the cell centers where the line-of-sight velocity vanishes is parallel to the limb. These lines are perpendicular to the limb for the toroidal component.
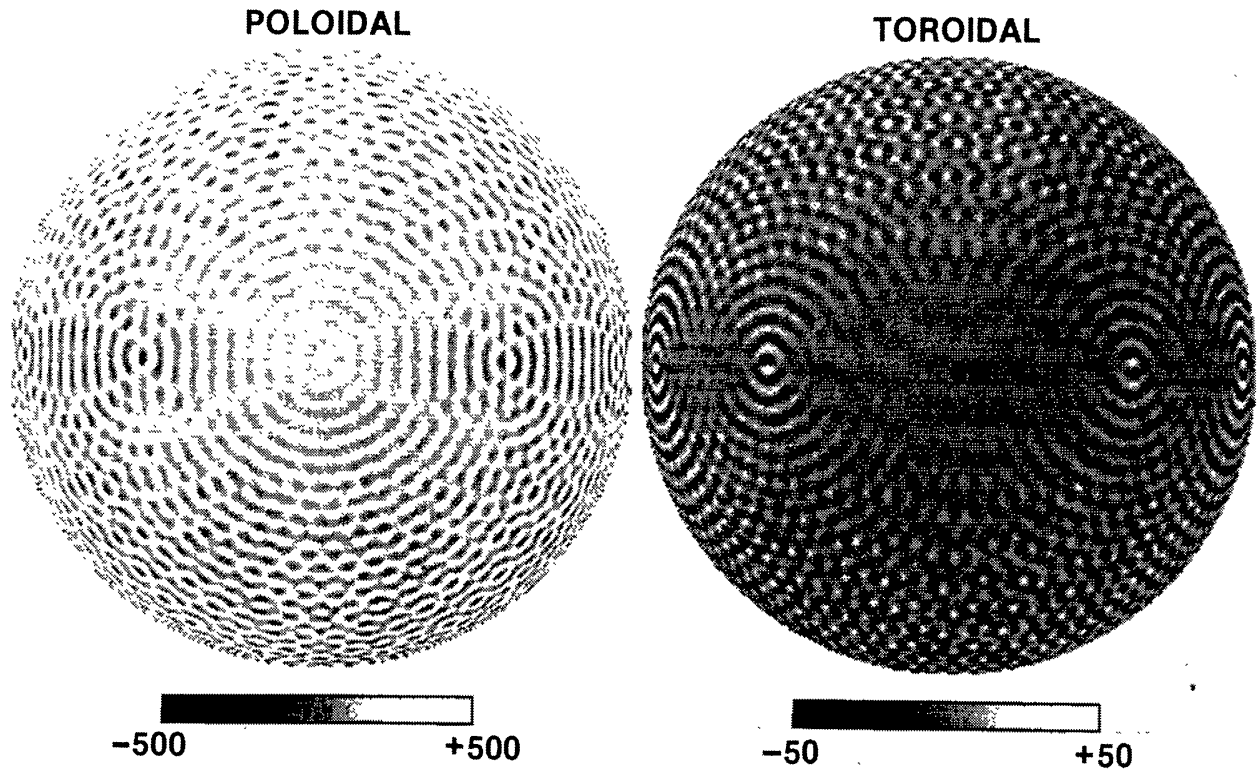

POLOIDAL   **TOROIDAL**

−500   +500   −50   +50

Fig. 1. The line-of-sight velocity for the poloidal and toroidal components of the synthetic supergranule spectrum. Light areas are approaching the observer, dark areas are receeding. The poloidal component represents overturning motions that carry fluid from updrafts to down drafts. The toroidal component represents spiraling motions around the updrafts and downdrafts.

The giant cells are represented in a similar manner but with $l = 24$, $m = 4, 8, 12, 16$, and 20 and amplitudes

$$S_{24}^m = 0.5, \qquad T_{24}^m = 0.5 . \tag{3.17}$$

The Coriolis force due to the Sun's rotation should introduce toroidal flows in association with the largely poloidal convective flows. Since the Coriolis force is more

important for large slow flows, relatively stronger toroidal components are used for the giant cells compared to those included in the supergranule signal. The line-of-sight component of the giant cell velocity field is shown in Figure 2. These cells do not closely resemble those found in numerical simulations of the solar convection zone (e.g., Gilman, 1977; Glatzmaier, 1984) but are simply larger versions of the supergranules with relatively stronger toroidal flows.
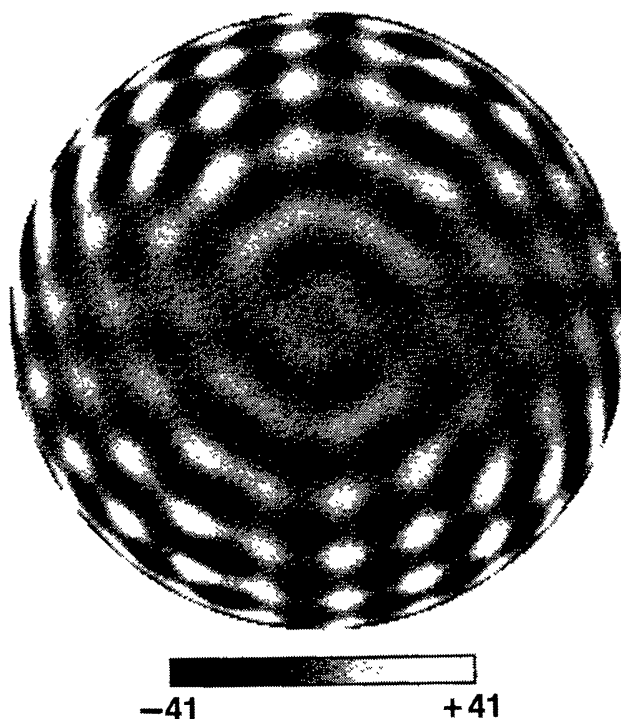

Fig. 2. The line-of-sight velocity pattern for the giant cells. This pattern is embedded in the synthetic data as a test of the success of the analysis technique in extracting large-scale, low-amplitude velocity features.

In constructing the synthetic data the vector velocities are calculated at each pixel by taking the sum of the different model components. The line-of-sight velocity is then calculated from

$$V(\theta, \phi) = U_\theta(\theta, \phi) \cos \theta \sin \phi + U_\phi(\theta, \phi) \cos \phi. \tag{3.18}$$

In addition to these velocity fields random noise can be added at each pixel to represent instrumental or observational sources of noise. It should be noted that in

constructing this synthetic data information about the spectrum is lost in the process by producing only the line-of-sight velocity component, by displaying only the one visible hemisphere of the Sun and by adding noise. The completed synthetic data image without noise is shown in Figure 3. The most obvious flows are the solar rotation and the supergranules. The other flow components, being much weaker, are well hidden by these stronger flow fields.

4. The Analysis Technique

In principle the analysis of the different velocity field components can proceed without regard to the order in which they are taken. In practice the analysis is cleaner if it is done in three sequential steps. First the limb shift is calculated and removed. The limb shift depends upon radial position from the disc center and thus is not tied to the spherical surface of the Sun. Since it is directly related to the position of the observer the analysis

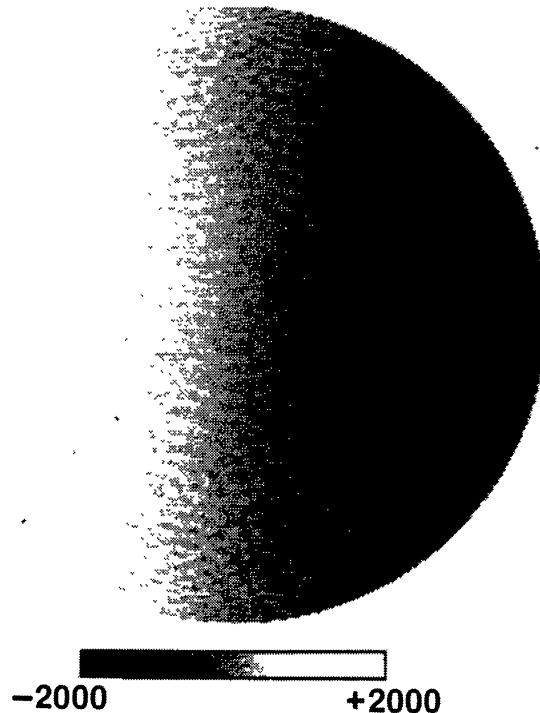**−2000**   **+2000**

Fig. 3. The synthetic data array constructed for testing the analysis technique. Rotation and supergranulation, the two strongest flows, are most evident. The meridional circulation and the giant cell pattern embedded in the data are not apparent.

for the limb shift is different and distinct from the analysis of the other velocity fields. Also, the limb shift and the meridional circulation signal are similar in some respects and rather difficult to separate. If the limb shift is calculated first, the meridional circulation analysis then proceeds more easily. In the second step the axisymmetric modes – rotation and meridional circulation are calculated and a correction is made to the limb shift. The third and final step is to find the convective modes, the supergranules and giant cells. This final step can proceed much faster if the original data is reformatted onto a grid with equally spaced data points in ϕ for each latitude band. However, this process introduces additional noise so the axisymmetic modes, which do not require this process, are calculated first.

4.1. THE LIMB SHIFT

The limb shift is assumed to be independent of latitude. This assumption may be flawed since there are indications (Beckers and Taylor, 1980; Brandt and Schröter, 1982) of a latitudinal dependence. However, even with a limb shift that is independent of latitude it is difficult to separate the limb shift and the meridional circulation. The effects due to latitudinal variations in the limb shift are deferred for later study.

The convective limb shift is found by calculating the average velocity at each radial position on the image. If there are $2N + 1$ pixels across the diameter of the image the data is bined into N equally spaced bins with radial position r_n. Since the number of points in each bin increases with r, the average velocity corresponds to a slightly offset position

$$\delta r_n = r_n - (n - 1)/(N - 1),\qquad(4.1)$$

where

$$r_n = \sum_{k=1}^{K} r_n(k)/K,\qquad(4.2)$$

with $r_n(k)$ being the radial position of the kth element in bin n. The average line-of-sight velocity for each bin,

$$\overline{V}_n = \sum_{k=1}^{K} \overline{V}_n(k)/K,\qquad(4.3)$$

is then corrected for this offset position using a second-order correction scheme

$$\overline{V}_n(\delta r = 0) = V_n(\delta r) - \left[\frac{\partial V_n}{\partial r}\right]\delta r - \frac{1}{2}\left[\frac{\partial^2 V_n}{\partial r^2}\right]\delta r^2\qquad(4.4)$$

to find the average velocity for the center of the bin.

An additional correction is required because of the curvature of this velocity profile. The average velocity in bin n is given by

$$\overline{V}_n = \frac{1}{\Delta r}\int_{r-\Delta r/2}^{r+\Delta r/2} V(r)\,\mathrm{d}r\qquad(4.5)$$

or

$$\overline{V}_n = V_n(0) + \left[\frac{\partial^2 V}{\partial r^2}\right]\frac{\Delta r^2}{24} \, , \qquad (4.6)$$

where Δr is the radial width of the bin. This gives a corrected value

$$V_n = \overline{V}_n - [\overline{V}_{n+1} - 2\overline{V}_n + \overline{V}_{n-1}]/24 \, . \qquad (4.7)$$

After these corrections are made the limb-shift profile still contains small scale variations due to the supergranules as well as elements due to the meridional circulation. To eliminate the small scale variations the profile is represented by a set of orthonormal polynomials, $L_n(r)$, with

$$V(r) = \sum_{n=1}^{n_{\max}} A_n L_n(r) \, . \qquad (4.8)$$

The coefficients A_n are then calculated from

$$A_n = \int_0^1 V(r)L_n(r) \, dr \, . \qquad (4.9)$$

Snodgrass (1984) has given the first few of these polynomials which are orthonormal over the interval $0 \le r \le 1$. This set is easily extended by the requirements of orthogonality and normalization.

The results of this analysis on the synthetic data is shown in Figure 4. The average velocity as a function of r is plotted with a thin line to illustrate he small-scale variations. A fifth-order polynomial representation of this curve is shown with a thick line through the data. The calculated velocity differs from that input for the limb shift (Equation (3.1)) by less than 3 m s^{-1}.

4.2. THE ROTATION PROFILE

The velocity field due to the solar rotation and differential rotation is given by

$$U_\phi^0(x) = \sum_l T_l^0[l(l+1)]^{1/2}\overline{P}_l^1(x) \, . \qquad (4.10)$$

So the line-of-sight velocity due to rotation is

$$V(x, \phi) = U_\phi^0(x) \cos \phi \, . \qquad (4.11)$$

Neglecting, for the moment, the other velocity components, the rotational velocity is given by

$$U_\phi^0(x) = \frac{2}{\pi} \int_0^\pi V(x, \phi) \cos \phi \, d\phi \, . \qquad (4.12)$$

The data is obtained on a grid with equal spacing in the plane of the sky, so this integral
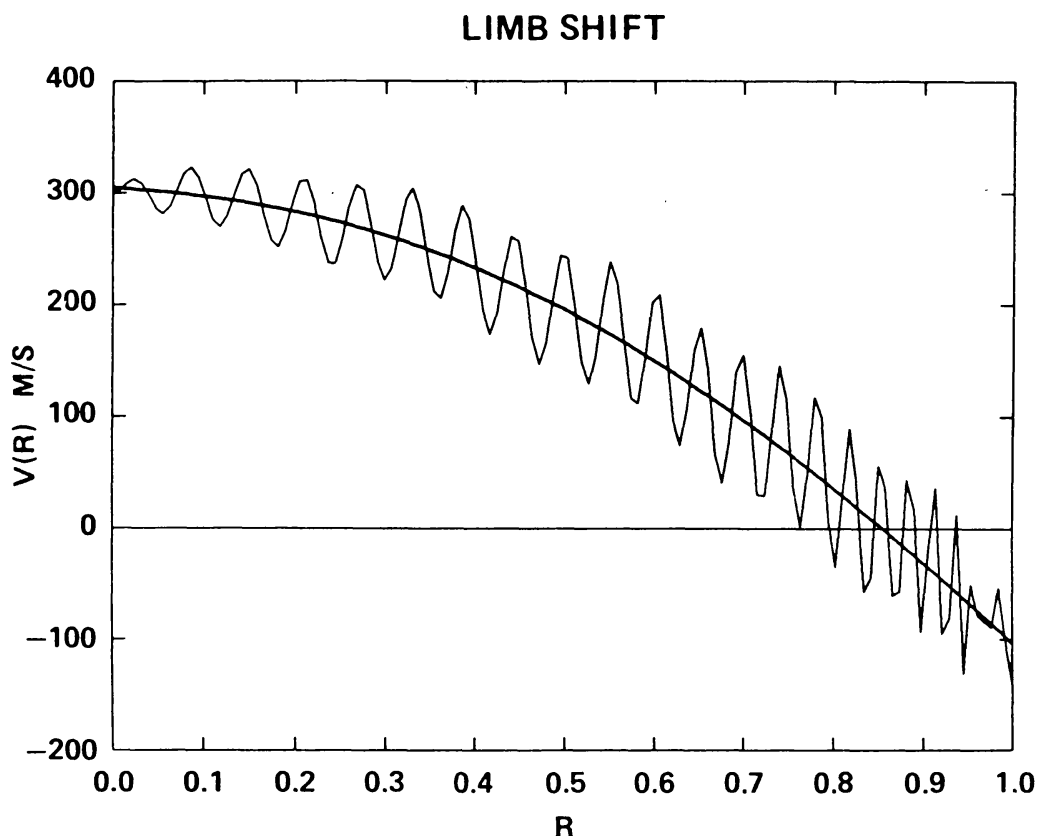
LIMB SHIFT

Fig. 4.   The results of the convective limb shift analysis. The thin curve is the average line-of-sight velocity, $V(r)$, as a function of radial distance, r, from disc center. The thick curve is the fifth-order polynomial representation of $V(r)$.

is somewhat difficult to calculate precisely. However, the integral can be transformed into the rectangular coordinate system and integrated by parts to give

$$U_\phi^0(x) = -\frac{2}{\pi} \int_{-\sin\theta}^{\sin\theta} \left[\frac{\partial V}{\partial y}\right] \sin\phi\,\mathrm{d}y\,, \qquad (4.13)$$

where y is measured westward from the central meridian and is normalized such that $y = 1$ on the west limb at the equator. The limits of the integration thus represent the east and west limb positions.

The spectral coefficients for the rotation are then calculated by taking the Legendre transform of $U_\phi^0(x)$ which gives

$$T_l^0 = [l(l + 1)]^{-1/2} \int_{-1}^{1} U_\phi^0(x)\,\overline{P}_l^1(x)\,\mathrm{d}x\,. \qquad (4.14)$$

The results of this analysis for the synthetic data are

$$T_1^0 = 1569.362\,, \qquad T_3^0 = -33.096\,, \qquad T_5^0 = -3.458\,, \qquad (4.15)$$

with all other coefficients smaller than 0.1 in magnitude. The rotation profile is shown
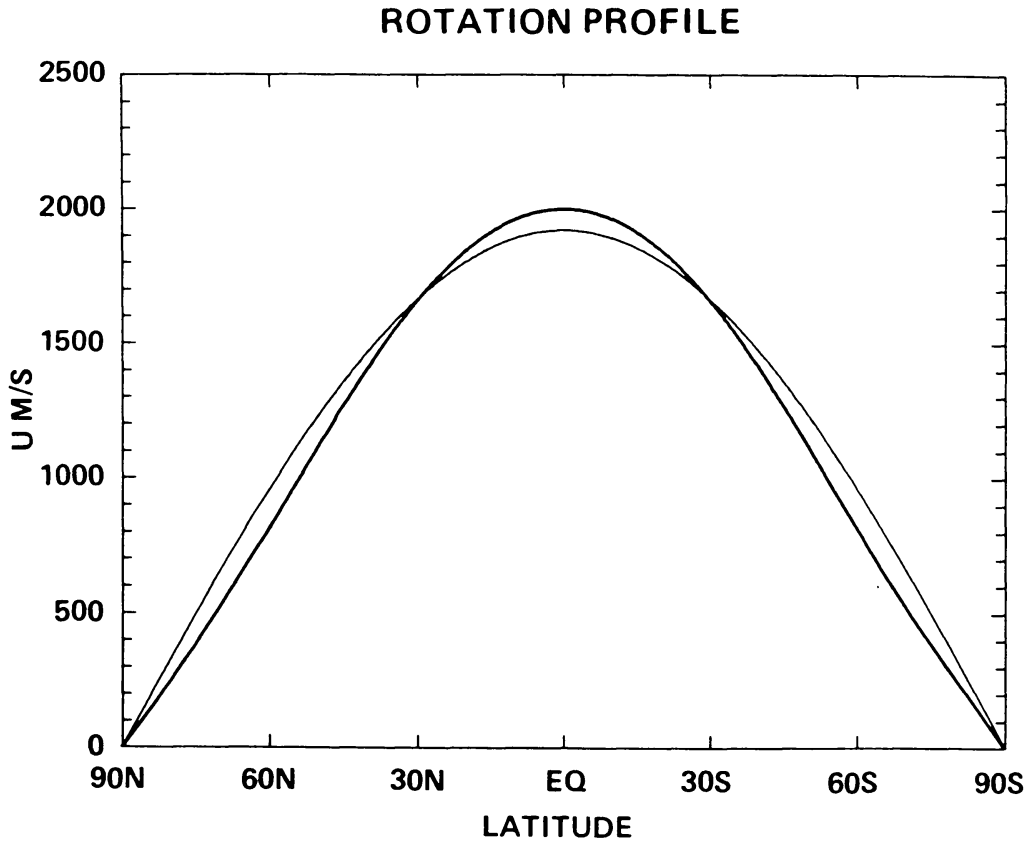
ROTATION PROFILE

Fig. 5. The rotation velocity as a function of latitutde. The thick curve is the measured rotation profile represented by spherical harmonic components with $l = 1$ to 16. The thin curve is the solid body rotation component, $l = 1$.

as a function of latitude in Figure 5. The full profile is represented by the thick line, the solid body component is shown with the thin line. On the scale shown here the measured values cannot be distinguished from the input profile; the differences are less than 1 m s^{-1}.

4.3. THE MERIDIONAL CIRCULATION

The meridional circulation velocity is given by

$$U_\theta^0(x) = - \sum_l S_l^0 [l(l+1)]^{1/2} \overline{P}_l^1(x) . \tag{4.16}$$

So the line-of-sight component is

$$V(x, \phi) = U_\theta^0(x) x \sin \phi . \tag{4.17}$$

Neglecting the other velocity components, the meridional flow is given by

$$U_\theta^0(x) x = \frac{2}{\pi} \int_0^\pi V(x, \phi) \sin \phi \, \mathrm{d}\phi . \tag{4.18}$$

Transforming this integral to one over the rectangular data array gives

$$U_\theta^0(x)x(1 - x^2)^{1/2} = \frac{2}{\pi} \int_{-\sin\theta}^{\sin\theta} V(x, y)\,\mathrm{d}y\,. \tag{4.19}$$

The spectral coefficients are again found by the Legendre transform with

$$S_l^0 = \frac{1}{(l + 1)}\left[\frac{(2l + 1)(2l - 1)}{l(l - 1)}\right]^{1/2} \int_{-1}^{1} U_\theta^0(x)x\overline{P}_{l-1}^1(x)\,\mathrm{d}x -$$

$$- \frac{(l - 2)}{(l + 1)}\left[\frac{(2l + 1)}{(2l - 3)}\right]^{1/2} S_{l-2}^0\,. \tag{4.20}$$

The meridional circulation and the limb shift are strongly mixed together in the line-of-sight velocity. In calculating the limb shift by taking average velocity measurements at different radii the even ($l = 2, 4, 6, \ldots$) meridional circulation components are folded into the limb shift signal. It can be shown that the odd components are not altered by the limb-shift analysis and that the even components are effected by only the even limb-shift polynomials. This coupling between the meridional circulation analysis and the limb-shift analysis is illustrated in Figure 6. When averages at different radial positions are taken in the limb-shift analysis they include contributions from the average of the meridional circulation components. The $l = 2$ component has a substantial average line-of-sight velocity while the $l = 3$ component has none. The response of unit amplitude meridional circulation components to the combined limb-shift/meridional circulation analysis can be calculated to give a response matrix, $R(l_1, l_2)$, where R is the resulting amplitude for the l_2 mode when the l_1 mode is input. This response matrix shows that $l_1 = 2$ gives zero for the $l_2 = 2$ coefficient and non-zero values for the higher, even l-coefficients. For $l_1 = 4$ the $l_2 = 4$ coefficient is reduced to 0.625 with some signal also appearing again in the higher even l-coefficients. This response matrix can be used to refigure the meridional circulation coefficients, S_l^0, given the coefficients, $S_l^{0'}$, calculated by the limb-shift/meridional circulation analysis. Since this analysis shifts the meridional circulation signal to higher wavenumbers the crucial part in recalculating the coefficients is to find S_2^0. This can be done by deviding the calculated coefficients for $l_2 = 4, 6, 8, \ldots$ by the response matrix coefficients for $l_1 = 2$ and taking an average:

$$S_2^0 = \frac{1}{N}\sum_{n=1}^{N} S_{2n+2}^{0'}/R(2, 2n + 2)\,. \tag{4.21}$$

The higher wavenumbers are then found using

$$S_{l_2}^0 = \frac{1}{R(l_2, l_2)}\left[S_{l_2}^{0'} - \sum_{l_1=2}^{l_2-2} R(l_1, l_2)S_{l_1}^0\right]\,. \tag{4.22}$$

After the meridional circulation spectrum is recalculated a correction must be made to the limb-shift profile which removes the meridional circulation contribution.
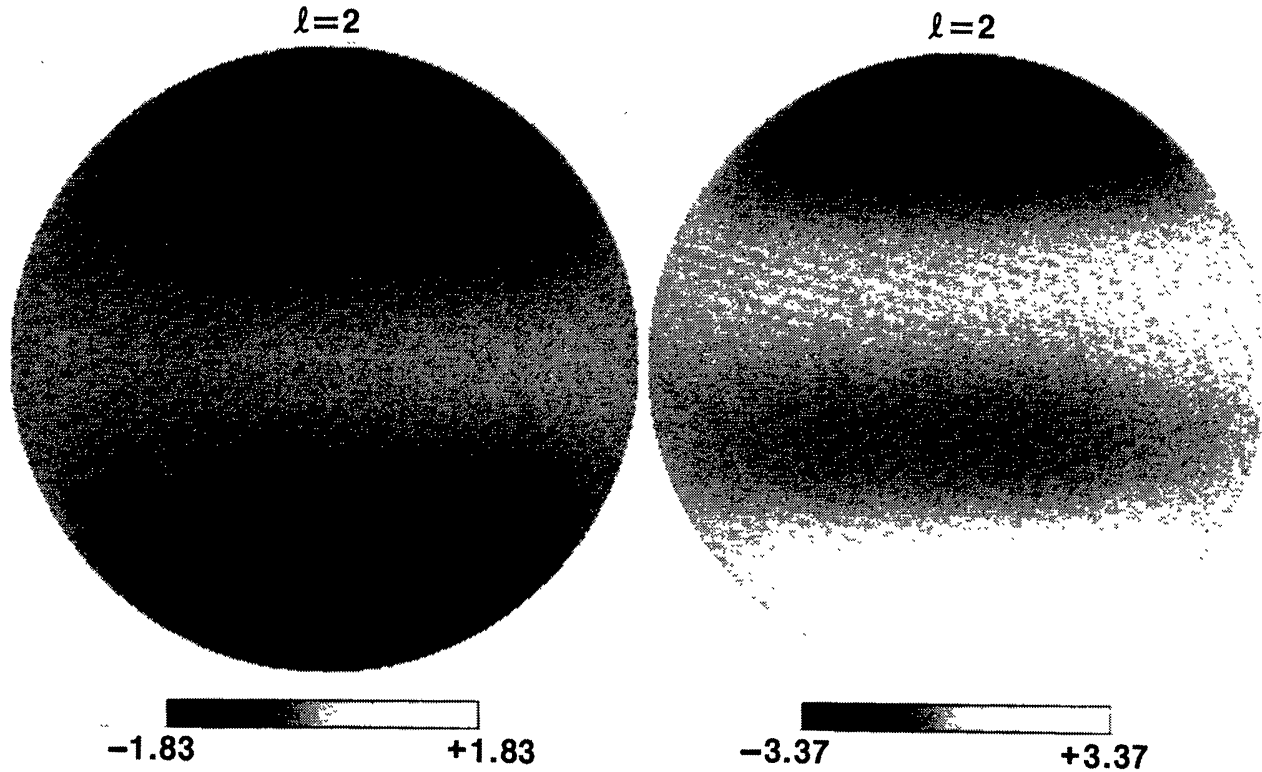
Fig. 6. The line-of-sight velocity for two meridional circulation components. The even, $l = 2$, component has an average velocity signal, $V(r)$, which is mixed with the limb-shift signal. The odd, $l = 3$, component does not mix with the limb shift. The meridional circulation analysis includes corrections for this mixing.

The results of the full meridional circulation analysis with the synthetic data gives

$$S_2^0 = 8.412\,, \qquad S_4^0 = 0.407\,, \qquad S_6^0 = -0.254\,, \qquad S_8^0 = 0.182\,.$$

$$(4.23)$$

The meridional circulation profile given by this spectrum is shown in Figure 7. The thick curve represents the calculated profile while the thin curve represents the input profile. Here, as with the limb-shift calculation, the small-scale variations are due to the supergranules and giant cells. It is worthwhile to note that this 20 m s^{-1} signal was extracted from data that had a dynamic range of $+2000 \text{ m s}^{-1}$ and yet the errors are only in the order of a few m s^{-1}.
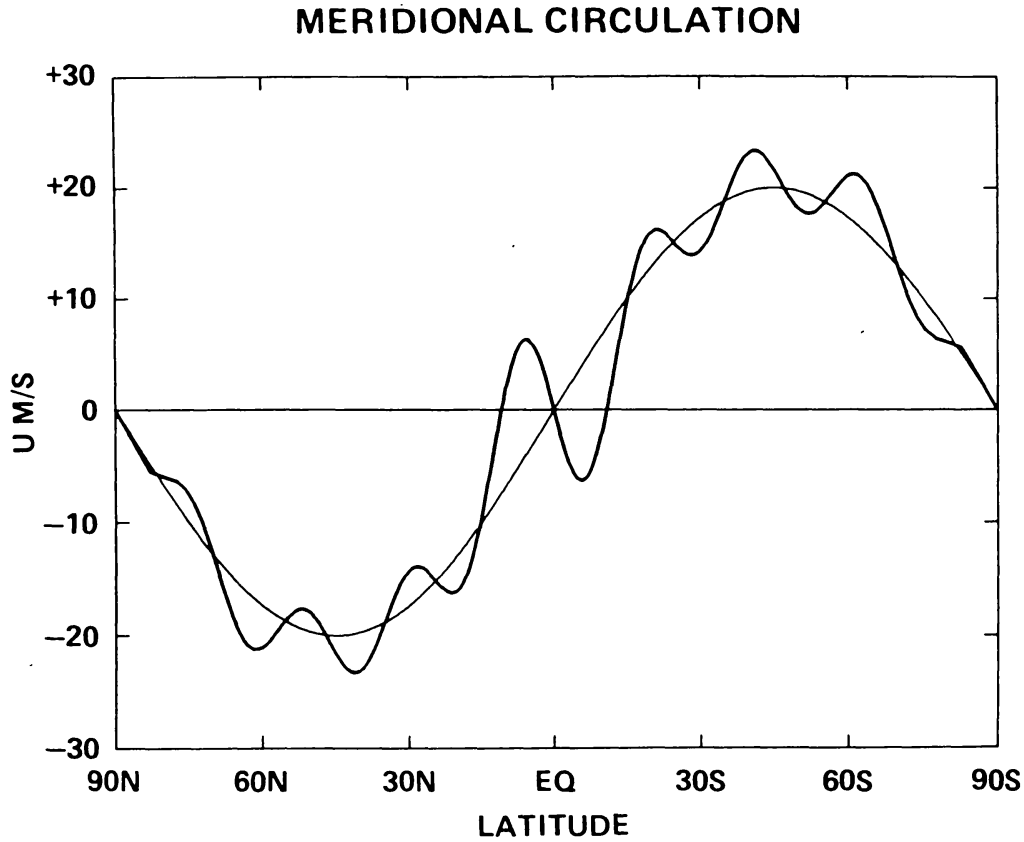
MERIDIONAL CIRCULATION

Fig. 7.   The meridional circulation velocity as a function of latitude. The thick curve is the measured velocity profile represented by sperical harmonic components with $l = 1$ to 16. The thin curve is the velocity profile that was embedded in the synthetic data.

4.4. THE CONVECTIVE MODES

For the nonaxisymmetric modes the two horizontal velocity components are given by

$$U_\theta(x, \phi) = \sum_{l=1}^{l_{max}} \sum_{m=0}^{l} [U_{\theta l}^m(x)]e^{im\phi} \qquad (4.24)$$

and

$$U_\phi(x, \phi) = \sum_{l=1}^{l_{max}} \sum_{m=0}^{l} [U_{\phi l}^m(x)]e^{im\phi}, \qquad (4.25)$$

where

$$U_{\theta l}^m(x) = (1 - x^2)^{-1/2} \left[\!\left[S_l^m \left\{ (2l+1)\left[\frac{(l+m+1)(l-m+1)}{(2l+3)(2l+1)}\right]^{1/2} \overline{P}_{l+1}^m(x) - \right.\right.\right.$$

$$\left.\left.\left. - (l+1)x\overline{P}_l^m(x)\right\} + T_l^m\{im\overline{P}_l^m(x)\} \right]\!\right] \qquad (4.26)$$

16   DAVID H. HATHAWAY

and

$$U^m_{\phi l}(x) = (1 - x^2)^{-1/2} \Bigg[S^m_l \{ im \overline{P}^m_l(x) \} -$$

$$- T^m_l \Bigg\{ (2l + 1) \left[\frac{(l + m + 1)(l - m + 1)}{(2l + 3)(2l + 1)} \right]^{1/2} \overline{P}^m_{l+1}(x) -$$

$$- (l + 1)x \overline{P}^m_l(x) \Bigg\} \Bigg] . \tag{4.27}$$

The line-of-sight component of this velocity field is obtained by using these components in Equation (3.18). This velocity field is analysed by first taking the Fourier transform of $V(x, \phi)$ over ϕ from 0 to π where

$$V^m(x) \equiv \frac{2}{\pi} \int_0^\pi V(x, \phi) e^{-im\phi} \, d\phi . \tag{4.28}$$

This gives

$$V^m(x) = \sum_{l=1}^{l_{max}} \Bigg\{ U^{m+1}_{\phi l} + U^{m-1}_{\phi l} + ix U^{m+1}_{\theta l} -$$

$$- ix U^{m-1}_{\theta l} + \frac{4i}{\pi} \sum_{m'=0}^l [(m' - m)^2 - 1]^{-1} \times$$

$$\times [(m' - m) U^{m'}_{\phi l} + ix U^{m'}_{\theta l}] \Bigg\}, \quad (m' - m) \text{ even} . \tag{4.29}$$

The last sum represents the mixing of modes due to the fact that only one hemisphere is seen (the Fourier integral is from 0 to π instead of 0 to 2π). This term gives a broad mixing between modes, with smaller contributions from modes with larger differences in azimuthal wavenumber. Note that this term is also present in the analysis for rotation and meridional circulation.

The second step is to take the Legendre transform for each order m where

$$V^m_l \equiv \int_{-1}^1 V^m(x) \overline{P}^m_l(x) \, dx . \tag{4.30}$$

This gives

$$V^m_l = [(l + m)(l - m + 1)]^{1/2} T^{m-1}_l + [(l - m)(l + m + 1)]^{1/2} T^{m+1}_l +$$

$$+ i \frac{(l - 1)}{[(2l + 1)(2l - 1)]^{1/2}} \{ [(l + m)(l + m - 1)]^{1/2} S^{m-1}_{l-1} +$$

$$+ [(l - m)(l - m - 1)]^{1/2} S^{m+1}_{l-1} \} +$$

$$+ i \frac{(l + 2)}{[(2l + 3)(2l + 1)]^{1/2}} \{ [(l - m + 1)(l - m + 2)]^{1/2} S^{m-1}_{l+1} +$$

$$+ [(l + m + 1)(l + m + 2)]^{1/2} S^{m+1}_{l+1} \} +$$

$$+ \sum_{l'} \sum_{m'} \left\{ \frac{4i}{\pi} [(m' - m)^2 - 1]^{-1} \int_{-1}^{1} [(m' - m)U^{m'}_{\phi l'}] \overline{P}^m_l(x) \, \mathrm{d}x \right\}.$$

(4.31)

Here, in addition to the mixing due to seeing only one hemisphere there is also a mixing between toroidal and poloidal components and between components with order differing by 2 due to the fact that only the line-of-sight component is measured.

The axisymmetric modes are found by taking $m = 1$ to get

$$V^1_l = [l(l + 1)]^{1/2} T^0_l + [(l - 1)(l + 2)]^{1/2} T^2_l +$$

$$+ i \frac{(l - 1)}{[(2l - 1)(2l + 1)]^{1/2}} \{[(l(l + 1)^{1/2} S^0_{l-1} +$$

$$+ [(l - 1)(l - 2)]^{1/2} S^0_{l-1}\} +$$

$$+ i \frac{(l + 2)}{[(2l + 3)(2l + 1)]^{1/2}} \{[l(l + 1)]^{1/2} S^0_{l+1} +$$

$$+ [(l + 2)(l + 3)]^{1/2} S^2_{l+1}\} + \sum_{l'm'} \{ \quad \}^{m'}_{l'},$$

(4.32)

where the last term corresponds to the double sum in (4.31). Although there is mixing with other modes due to the previously mentioned effects, the toroidal (rotation) and poloidal (meridional circulation) components are cleanly separated into the real and imaginary parts of V (both T and S are real or $m = 0$). In spite of this mixing between the different modal components the supergranules and giant cells can be separated using this type of analysis. After calculating the V^m_l the giant cell pattern can be reproduced by constructing the velocity field using

$$V(\theta, \phi) = \sum_{l=1}^{l_{\max}} \sum_{m=0}^{l} V^m_l \overline{P}^m_l(\cos \theta) e^{im\phi},$$

(4.33)

where $l_{\max}$ is a maximum wavenumber chosen to separate giant cells from supergranules. The results of this analysis for the synthetic data is shown in Figure 8 for $l_{\max} = 32$. The resulting giant cell pattern is easily recognized as that shown in Figure 2. The differences between the pattern embedded in the synthetic data and this extracted signal are on the order of a few m s^{-1}. Here again it should be noted that this pattern was extracted from data that also included supergranules with 500 m s^{-1} velocities.

4.5. EFFECTS DUE TO RANDOM NOISE

Noise is introduced in the synthetic data by adding random numbers with a pre-determined range in amplitude at each pixel. This represents random noise with zero-correlation length which might be due to either instrumental or to observational effects (e.g., fluctuations in the number of granules in a picture element). Several different levels of noise were introduced in the synthetic data and the analysis programs were then run to determine the effects of these different noise levels.
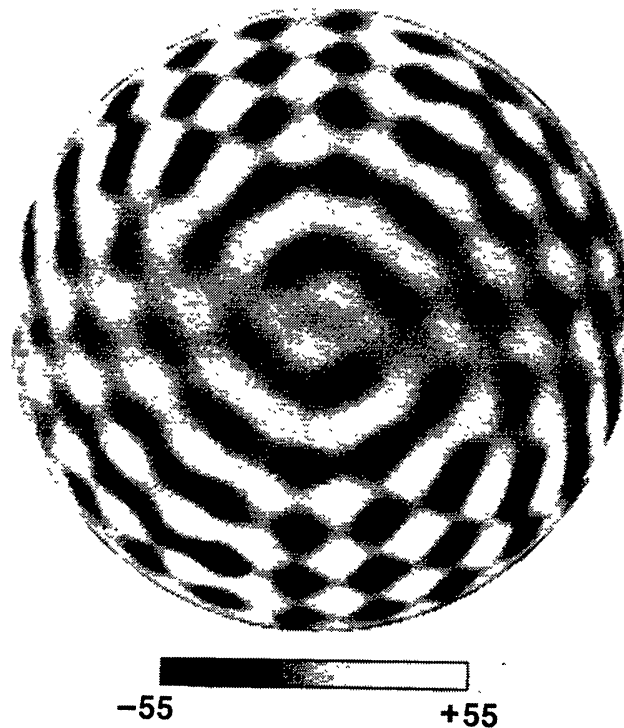
Fig. 8.   The giant cell pattern extracted from the synthetic data by the spherical harmonic analysis technique. This pattern is nearly identical to that shown in Figure 2 except for small variations in amplitude.

At a noise level of 10 m s^{-1} the changes were very slight. The coefficients for the rotation and meridional circulation components were virtually unchanged except for the addition of a background level of about 0.02 throughout the spectrum. For the giant cell analysis this contribution does produce small changes in the extracted pattern since this represents a more substantial relative contribution to these modes.

At a noise level of 100 m s^{-1} the changes are more obvious. At this noise level the background noise in the spectrum is on the order of 0.2. This still gives minor changes to the rotation and meridional circulation spectra since the input coefficients were much larger, but the contribution is large enough to produce changes in the meridional circulation profile on the order of a few m s^{-1}. This spectral noise is more severe for the giant cells since they had coefficients of 0.5. The extracted giant cell patterns are shown in Figure 9. For 10 m s^{-1} noise the patterns is hardly changed from the zero noise level pattern shown in Figure 8. For 100 m s^{-1} the embedded giant cell pattern is difficult to recognize.

10 m/s NOISE LEVEL   **100m/s NOISE LEVEL**

−56   +56   −86   +86
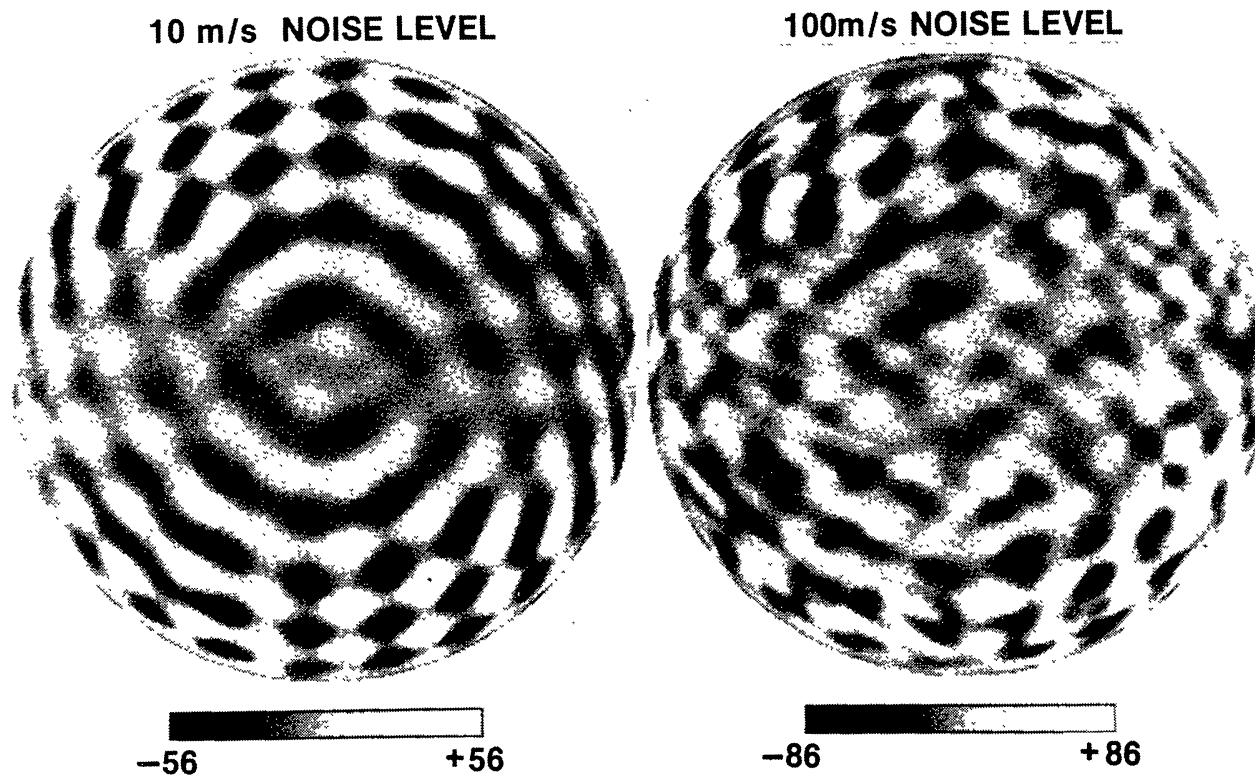
Fig. 9.   The giant cell patterns extracted from the synthetic data when random noise is included in the data. For a 10 m s^{-1} noise level the changes in the pattern are relatively small. For a 100 m s^{-1} noise level the changes are quite severe although some features from the original pattern are visible.

5. Conclusions

The spherical harmonic analysis technique presented here promises to be an accurate and powerful technique for analysing steady flows in the solar photosphere. The solar differential rotation profile can be accurately measured on an hourly or daily basis so that secular changes can be observed. The meridional circulation can be separated from the limb shift and accurately measured if the limb shift does not depend upon latitude. The limb shift itself can be accurately measured. Giant cells with small amplitude flows can be separated from supergranules, again on an hourly basis. Truely random noise, as opposed to the 'noise' due to supergranules, makes identifying giant cells difficult only when the noise level begins to exceed the signal level for the giant cells.

    Although the analysis is designed to use hourly observations, the results of the analysis would be strengthened by observing for extended periods. In searching for giant cells the analysis would have to be extended over the course of several days. To be identified as giant cells the extracted patterns must persist from hour to hour and rotate at the solar rate from day to day. Extended observations would also give a better determination of the spectral coefficients for the rotation and meridional circulation by

simply providing a series of coefficients that would be averaged to reduce fluctuations.

Further study is needed on some aspects of the analysis technique. It was assumed that the solar rotation axis was in the plane of the sky when in fact it can be tilted toward or away from the observer by as much as 7.15°. For the rotation profile this tilt can be largely corrected by simply dividing the velocities by the cosine of the B angle. For the other flow components, and for a more accurate representation of the rotation component, a more formal change of axis for the spherical harmonics must be used. It was also assumed that the limb shift was independent of latitude. Relaxing this assumption may change some aspects of the analysis for the limb shift and for the meridional circulation. These aspects, and the use of multiple viewing angles to reduce the mixing between modes, will be deferred for later study.

This analysis technique is a natural companion to helioseismology studies. It uses the same data sets and observation techniques as well as much of the same analysis techniques. As helioseismology tools such as the Solar Oscillation Imager on the Solar and Heliospheric Observatory (SOHO) and the Global Oscillations Network Group (GONG) telescopes become available, this technique should prove to be valuable for analysing the steady components of flows in the solar photosphere

Acknowledgements

References

Abramowitz, M. and Stegun, I. A.: 1964, *Handbook of Mathematical Functions*, Natl. Bureau of Standards.
Beckers, J. M. and Taylor, W. R.: 1980, *Solar Phys.* **68**, 41.
Brandt, P. N. and Schröter, E. H.: 1982, *Solar Phys.* **79**, 3.
Bumba, V. and Howard R.: 1965, *Astrophys. J.* **141**, 1502.
Chandrasekhar, S.: 1961, *Hydrodynamic and Hydromagnetic Stability*, Clarendon Press, Oxford.
Gilman, P. A.: 1977, *Geophys. Astrophys. Fluid Dynam.* **8**, 93.
Glatzmaier, G. A.: 1984, *J. Comput. Phys.* **55**, 461.
Hathaway, D. H.: 1982, *Solar Phys.* **77**, 341.
Hill, F.: 1986, private communication.
Howard, R. F. and Harvey, J.: 1970, *Solar Phys.* **12**, 23.
Howard, R. F. and LaBonte, B. J.: 1980, *Astrophys. J.* **239**, L33.
Simon, G. W. and Weiss, N. O.: 1968, *Z. Astrophys.* **69**, 435.
Snodgrass, H. B.: 1984, *Solar Phys.* **94**, 13.
Stenflo, J. O. and Vogel, M.: 1986, *Nature* **319**, 285.
Worden, S. P. and Simon, G. W.: *Solar Phys.* **46**, 73.